Article

Atomic dynamics of electrified solid–liquid interfaces in liquid-cell TEM

https://doi.org/10.1038/s41586-024-07479-w

Received: 15 August 2023

Accepted: 26 April 2024

Published online: 19 June 2024

Check for updates

Qiubo Zhang[1,8], Zhigang Song[2,8], Xianhu Sun[1,8], Yang Liu[3,8], Jiawei Wan[1,4], Sophia B. Betzler[1], Qi Zheng[1], Junyi Shangguan[1], Karen C. Bustillo[5], Peter Ercius[5], Prineha Narang[6,7], Yu Huang[3] & Haimei Zheng[1,4]✉

Electrified solid–liquid interfaces (ESLIs) play a key role in various electrochemical processes relevant to energy[1–5], biology[6] and geochemistry[7]. The electron and mass transport at the electrified interfaces may result in structural modifications that markedly influence the reaction pathways. For example, electrocatalyst surface restructuring during reactions can substantially affect the catalysis mechanisms and reaction products[1–3]. Despite its importance, direct probing the atomic dynamics of solid–liquid interfaces under electric biasing is challenging owing to the nature of being buried in liquid electrolytes and the limited spatial resolution of current techniques for in situ imaging through liquids. Here, with our development of advanced polymer electrochemical liquid cells for transmission electron microscopy (TEM), we are able to directly monitor the atomic dynamics of ESLIs during copper (Cu)-catalysed CO_2 electroreduction reactions (CO_2ERs). Our observation reveals a fluctuating liquid-like amorphous interphase. It undergoes reversible crystalline–amorphous structural transformations and flows along the electrified Cu surface, thus mediating the crystalline Cu surface restructuring and mass loss through the interphase layer. The combination of real-time observation and theoretical calculations unveils an amorphization-mediated restructuring mechanism resulting from charge-activated surface reactions with the electrolyte. Our results open many opportunities to explore the atomic dynamics and its impact in broad systems involving ESLIs by taking advantage of the in situ imaging capability.

Extensive studies of ESLIs have been on the physisorption[8] and chemisorption[9] of species at or near the interfaces. However, the microscopic details of ESLIs, especially their atomic-scale structural evolution during electrochemical reactions, remain unclear. In electrocatalysis, such as in Cu-catalysed CO_2ERs, notable surface restructuring and dissolution of catalysts may occur at the ESLI[1,10]. Nevertheless, mechanisms underlining the structural modifications are not well understood owing to technical challenges in direct probing the atomic dynamics of ESLIs. Advanced in situ methods, such as Raman spectroscopy[11,12], X-ray scattering techniques[13,14], vibrational spectroscopy[15], infrared reflection absorption spectroscopy[16], scanning tunnelling microscopy[17] and others, have been used to study various ESLIs of flat surfaces or nanoparticle ensembles during electrochemical reactions. In situ TEM allows the tracking of individual nanocatalyst evolutions during reactions[18–20], but the spatial information has so far been limited to imaging through liquids under electric biasing[10,21–24]. Here we introduce our newly developed high-resolution electrochemical polymer liquid cells (PLCs) that have enabled groundbreaking atomic-resolution imaging of ESLIs in electrochemical reactions. With this development, we show previously unseen liquid-like interphase and atomic dynamics of ESLIs during CO_2ERs.

Fluctuating amorphous interphase at ESLIs

We conducted the Cu-catalysed CO_2ER experiments by PLC (Extended Data Fig. 1 and Supplementary Figs. 1 and 2). Figure 1a shows a single electrolyte pocket within the electrochemical PLC, in which a Cu nanowire is connected to the Pt cathode, as confirmed by the high-angle annular dark-field (HAADF) image in Fig. 1b. The redox potential and current–potential curves measured through the electrochemical liquid cell indicate that the electrochemical PLC functions well (Supplementary Fig. 3). We monitor the interfaces between the Cu catalyst and electrolyte under electrochemical conditions in the PLC (Supplementary Figs. 4 and 5). Following the applied potential, a fluctuating liquid-like amorphous structure is observed on the Cu nanowire surface. It fluctuates with cyclic disappearance and occurrence (Fig. 1c and Supplementary Videos 1 and 2). The high-resolution image (Fig. 1d) highlights notable features that distinguish the amorphous interphase from both the crystalline Cu and the electrolyte. The interface between the amorphous interphase and the electrolyte seems smooth, whereas the interface with the crystalline Cu is rough, with atomic steps.

[1]Materials Sciences Division, Lawrence Berkeley National Laboratory, Berkeley, CA, USA. [2]Harvard John A. Paulson School of Engineering and Applied Sciences, Harvard University, Cambridge, MA, USA. [3]Department of Materials Science and Engineering, University of California, Los Angeles, Los Angeles, CA, USA. [4]Department of Materials Science and Engineering, University of California, Berkeley, Berkeley, CA, USA. [5]National Center for Electron Microscopy, Molecular Foundry, Lawrence Berkeley National Laboratory, Berkeley, CA, USA. [6]Division of Physical Sciences, College of Letters and Science, University of California, Los Angeles, Los Angeles, CA, USA. [7]Department of Electrical and Computer Engineering, University of California, Los Angeles, Los Angeles, CA, USA. [8]These authors contributed equally: Qiubo Zhang, Zhigang Song, Xianhu Sun, Yang Liu. ✉e-mail: hmzheng@lbl.gov

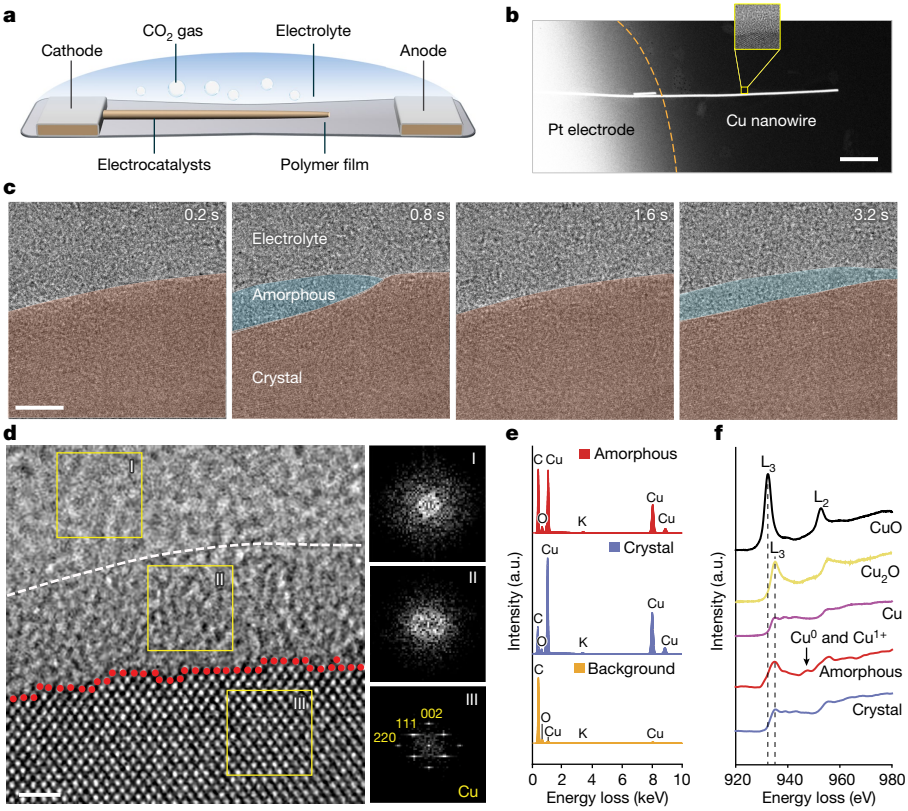

Fig. 1 | Experimental setup and characterization of the fluctuating liquid-like amorphous interphase. a, Schematic of a perspective view of the sample area. **b**, HAADF image of a Cu nanowire suspended on the Pt electrode. The inset highlights the ESLI. **c**, A TEM image sequence shows the emergence and fluctuations of the amorphous interphase (raw data in Supplementary Fig. 28). **d**, HRTEM image and corresponding fast Fourier transform patterns (I, II, III) show distinguishing structure and contrast features of the amorphous interphase, crystal Cu and electrolyte. **e**, EDS spectra of amorphous interphase, crystal Cu and electrolyte. **f**, Cu $L_{2,3}$ edge EELS spectra of different phases. Scale bars, 500 nm (**b**), 5 nm (**c**), 1 nm (**d**). a.u., arbitrary units.

Our control experiments show that, under identical electron-beam irradiation conditions, without biasing, there is no such amorphous interphase (Supplementary Fig. 6 and Supplementary Video 3). Furthermore, ex situ H-cell electrochemical experiments also verify the formed amorphous at the surface of Cu nanowires after electrochemical activation (Supplementary Figs. 7–17). Ex situ flow-cell experiments revealed that Cu catalyst exhibited a stepped surface post-CO_2ER testing, which is reminiscent of that observed in H cells, implying similar reconstruction of catalyst surfaces (Supplementary Fig. 18), therefore the generation of amorphous structures at the ESLI is intrinsic under electrochemical conditions. By contrast, electron-beam irradiation promotes crystallization of the amorphous interphase to form $Cu(OH)_2$ and Cu_2O nanocrystals (Supplementary Figs. 19–21), which further excludes electron-beam-induced amorphization.

As well as the structure information, our PLC allows rapid cooling to the cryogenic temperature to freeze the activated amorphous interphase, indicating diverse applications of our PLC nanoplatforms. The energy-dispersive X-ray spectroscopy (EDS) and electron energy loss spectroscopy (EELS) of the frozen amorphous interphase enable the composition and valence states analysis (Fig. 1e,f and Supplementary Figs. 22–27). Our control experiments with high-resolution transmission electron microscopy (HRTEM) imaging (Supplementary Figs. 19–21) indicate that the amorphous interphase comprises Cu, O and H. This is attributed to the fact that the elements present in the formed nanocrystals can only originate from the amorphous interphase layer. The EDS spectra further confirm the presence of Cu in the amorphous interphase (Fig. 1e). Furthermore, by comparing the C-to-O ratio in the amorphous layer and the crystalline Cu segment, we also find the presence of C in the amorphous layer. Therefore, we summarize that Cu, C, H and O have been identified in the amorphous interphase. EELS spectra (Fig. 1f and Supplementary Table 1) show that the amorphous interphase contains both Cu^0 and Cu^{1+}. Using the multiple linear least squares fitting method[25], we estimate the ratio of Cu^0 to Cu^{1+} and the results indicate that the ratio of Cu^0 to Cu^{1+} increases when the position is closer to the amorphous–crystalline Cu interface (Supplementary Figs. 24–27). On the basis of the above chemical analysis, we can conclude that the amorphous interphase is a complex containing Cu^0 and Cu^{1+}.

The amorphous interphase experiences two types of dynamic behaviour (Fig. 2a): (1) it flows along the crystalline Cu surfaces; (2) the amorphous interphase and crystalline Cu interconvert with each other, by which the original smooth surfaces of the crystalline Cu become rough (Supplementary Figs. 28–30). A representative scenario showing the flow behaviour can be seen in Fig. 2b, in which the red arrows highlight the lateral motion of an amorphous interphase exhibiting fluidity (Supplementary Video 4). The liquid-like amorphous interphase structure enters the field of view from the left region (0.6 s), diffuses along the crystalline Cu surface from left to right (0.6–3.0 s) and exits to the right (3.0 s). For quantification, we plot the projected area of crystalline Cu and amorphous interphase versus time (Extended Data Fig. 2a). The large changes in the projected area of amorphous interphase correspond to its lateral flow along the interface. The interconversion between two phases can be distinguished (as indicated by the opposite trend of the two plots at 1–2 s), but it is not important in this scenario.

Substantial interconversion between the amorphous interphase and crystalline Cu can be seen in Fig. 2c (Supplementary Video 5). As indicated by the yellow arrows, the amorphous interphase grows into the crystalline Cu. Then it shrinks gradually until it has completely disappeared, as highlighted by the blue arrows. The projected area changes of the two phases over time clearly show opposite trends and comparable magnitudes, demonstrating the predominant interconversion

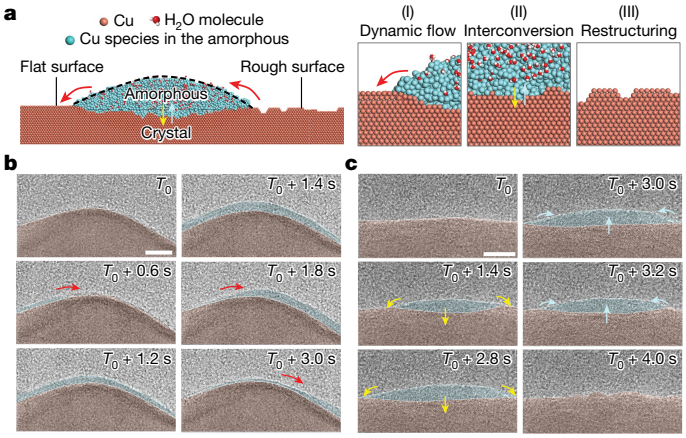

Fig. 2 | Dynamic behaviour of liquid-like amorphous interphase. a, The schematic shows that the amorphous interphase mediates the crystalline Cu surface restructuring through dynamic flow and interconversion behaviours. **b**, HRTEM images show the liquid-like flow of the amorphous on the crystalline Cu surface. Scale bar, 5 nm. **c**, HRTEM images show the interconversion between crystalline Cu and amorphous interphase. Scale bar, 5 nm. False colours in **b** and **c** are used to guide the eye (original images are provided in Supplementary Figs. 29 and 30).

behaviour (Extended Data Fig. 2b). By comparing the TEM images at 0 s and 4.0 s (Fig. 2c), we also find that the original smooth surface of the crystalline Cu becomes rough. This is largely induced by inhomogeneous mass redistribution under the electrochemical redox reactions (detailed in Fig. 3d).

Interphase-tuned surface restructuring

To gain a deep understanding of how the liquid-like amorphous interphase activates and roughens the crystalline Cu surface, we trace the dynamic evolution of ESLIs at the atomic level. As shown in Fig. 3a (Supplementary Video 6), the crystalline surface covered by the amorphous interphase experiences more severe dissolution of Cu than the bare surface. Three distinct features of the ESLI can be identified. First, the interface between the amorphous interphase and electrolyte is smooth, as indicated by the yellow dashed line. Second, the interface between the crystalline Cu and electrolyte seems smooth and atomically flat. Third, the interface between the crystalline Cu and amorphous interphase is rough, with atomic steps, pits and ridges.

At the interface between crystalline Cu and electrolyte, Cu atoms can be removed from the atomic terrace, but the resulting vacancies are rapidly refilled, leading to a smooth and atomically flat surface again (Extended Data Fig. 3). Thus, this type of atomic displacement at the atomic terrace has a negligible impact on the crystalline Cu surface restructuring and mass dissolution. However, at the triple-phase junction (Fig. 3b,c and Supplementary Video 7), Cu atoms are primarily removed along atomic steps (0–0.9 s), owing to the lower vacancy-formation energy at these locations. Individual or numerous Cu atoms could be detached at the atomic steps. Our density functional theory (DFT) calculations (Supplementary Table 2) show that the vacancy-formation energy is lower at the atom steps (2.51 eV) than that at the atomic terrace (2.914 eV). For the electrified interfaces (for example, with the influence of surface electrons), the formation energy of vacancies at the atomic steps can be further reduced, leading to the predominant removal of Cu atoms along the atomic steps. Also, several Cu atoms can be removed simultaneously along the atomic steps assisted by the adsorption of molecules (for example, the vacancy-formation energy of 1.41 eV with molecule adsorption on several Cu atoms versus 4.22 eV without molecule adsorption) (Supplementary Table 2).

At the interface between the crystalline Cu and the amorphous interphase, the removal of Cu atoms is more pronounced and seems random (Fig. 3b; see also Supplementary Video 8). As well as step atoms and isolated adatoms that can be easily removed (Extended Data Fig. 4 and Supplementary Video 9), Cu atoms on the terrace can also be readily dragged away. Figure 3d shows that the original terrace is intact (0 s). After 0.1 s, several atoms are lifted and moved from the positions indicated by the dashed yellow dots to the solid yellow dots.

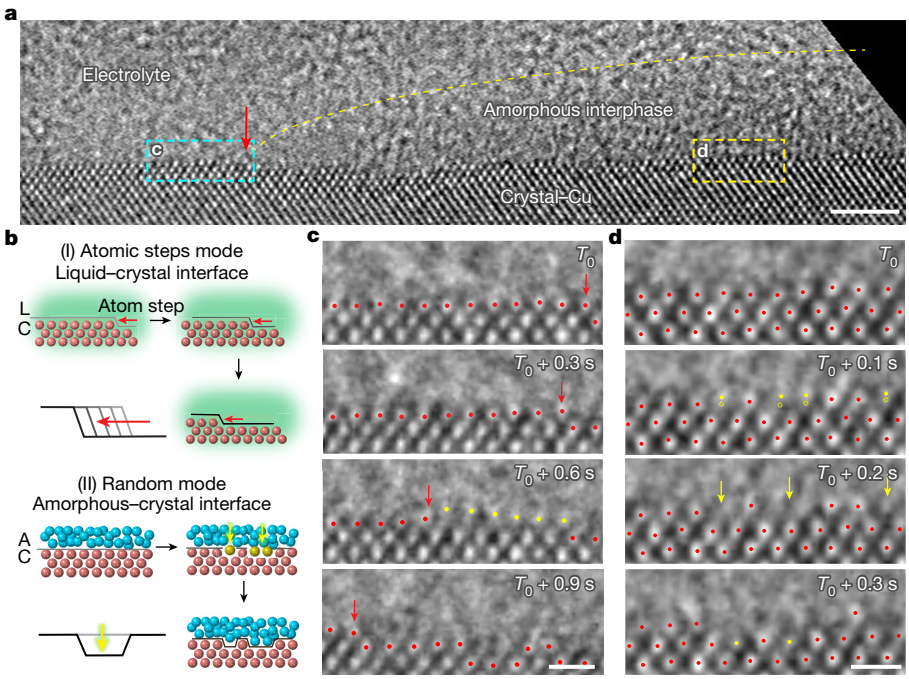

Fig. 3 | The atomic dynamics of Cu restructuring and dissolution at the ESLI. a, HRTEM image shows three types of interfaces. Scale bar, 2 nm. **b**, Schematic illustration of two distinct atom detachment modes: atomic steps mode and random mode. **c**, HRTEM images show the atomic-step-dependent detachment of Cu atoms at the triple-phase junction. Scale bar, 5 Å. **d**, HRTEM images show the random detachment of Cu atoms at the interface between crystalline Cu and amorphous interphase. Scale bar, 5 Å.

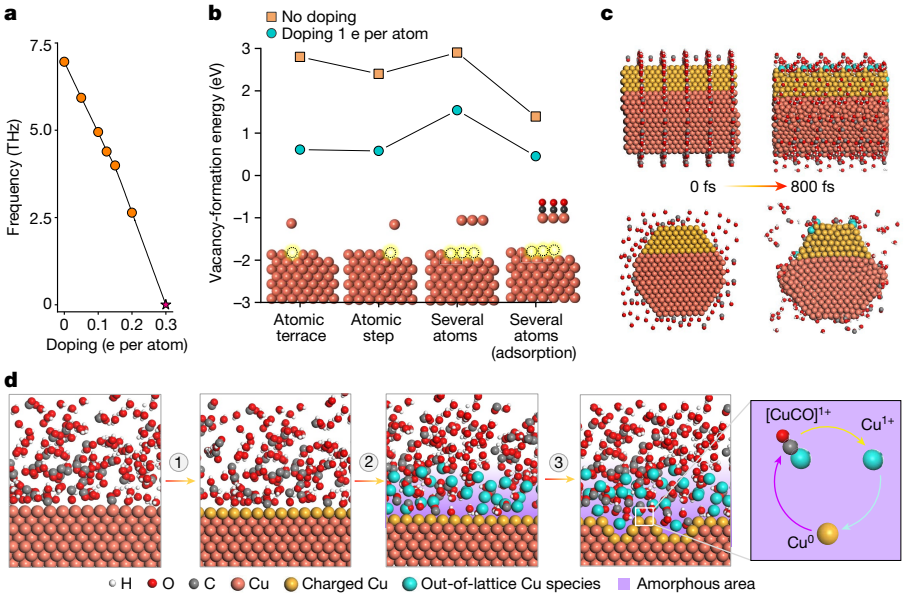

Fig. 4 | Proposed mechanism of amorphous interphase formation and crystalline Cu surface restructuring. a, Maximum phonon frequency of bulk Cu varies with different levels of electron doping concentration. When a negative frequency appears, the maximum phonon frequency is set as 0 and labelled by a star. **b**, Cu vacancies formation energies at various sites with electronic doping (1 e per atom) or without doping. **c**, Snapshot of initial and final structure (800 fs) with electron doping of 0.5 e per atom at the upper part of the nanowire. Upper panels are side views and lower panels are cross-sectional views. Doped zones are highlighted in yellow. To show the nanowire shape, the geometry is artificially extended by five periods in the axial direction. **d**, Schematic illustration of the restructuring process of crystalline Cu surface, including activation of the surface atoms, dissolving of Cu and combination with solvent molecules, and reversible transformation between amorphous interphase and crystalline Cu. Notably, specific to the Cu-catalysed CO_2ER, CO is chosen as the representative adsorbed molecule in our calculations to illustrate the formation of amorphous interphase. Other adsorbed molecules (such as *H, *OCHO, *CO_3, *C_2H_4 etc.) may also react with Cu to form the amorphous phase.

Then these atoms are moved into the amorphous interphase, leaving atomic pits at their original positions (0.2 s), as marked by the yellow arrows. Furthermore, Cu atoms in the second layer can also be removed (0.3 s), despite the unfinished detachment of the first layer (Fig. 3d and Extended Data Fig. 5). Thus, the random removal of atoms at the interface between the crystalline Cu and the amorphous interphase results in a rough interface, consistent with DFT calculation results of the similar Cu vacancy-formation energies on the terrace (0.61 eV) and at steps (0.58 eV) (Supplementary Table 2).

Mechanism of the interphase formation

Theoretically, during electrochemical processes, an electric double layer forms at the ESLI, exerting control over the kinetics and thermodynamics of interfacial reactions (Supplementary Fig. 31). According to previous reports, the dielectric constant of water is approximately 78.4 times that of vacuum and the induced charge concentration at metal surfaces is on the order of around 10^{23} e cm^{-3} (0.5 e per atom) in magnitude[26]. Molecular dynamics simulations show that electron doping is the primary factor inducing the amorphization of metal surface atoms (Supplementary Fig. 32–35). Electron doping can reduce atom–atom interaction in metal surfaces, weakening metallic bonds, which activate surface atoms to interact with the electrolyte, forming amorphous complexes.

For the Cu-catalysed CO_2ER, we calculated phonon dispersion under various electron doping densities (0–1 e per atom). Our calculations show that phonon band dispersion decreases with increasing electron doping (Fig. 4a and Extended Data Fig. 6). When the value of electron doping density reaches 0.3 e per atom, the phonon band structure shows negative frequencies, suggesting that the material is unstable. The DFT calculation shows that Cu with electron doping has a lower vacancy-formation energy than that without electron doping (Fig. 4b). Thus, the Cu surface atoms with a high electron doping density are more likely to be solvated under the interactions with molecules in solution, such as *H, *OH *OOH, *CO, *OCHO, *C_2O_4 and *HCO_3 (* denotes adsorbed)[27]. Here we chose CO as the representative adsorbed molecule in our calculations to illustrate the formation of amorphous interphase at the ESLI. Our DFT simulations demonstrate that, with electron doping, the Cu atoms on the nanowire surfaces are solvated (as depicted by the blue balls in Fig. 4c and Extended Data Fig. 7), whereas without electron doping, the Cu nanowire maintains its crystal lattice after 800 fs, even at 1,000 K (Supplementary Fig. 36).

On the basis of the above calculations and our experimental observations, we propose a mechanism of amorphous interphase formation. As illustrated in Fig. 4d, under a negative potential, Cu atoms at the nanowire surfaces become charged and activated. Adsorbed molecules (for example, the representative CO) in the electrolyte can be adsorbed on the activated Cu atoms, which may result in the dissolution of Cu (Fig. 3c,d) and the formation of $[CuCO]^+$ complex[27]. The inherent instability of $[CuCO]^+$ complex leads to spontaneous dissociation into Cu^+ and CO (ref. 28). The Cu^+ ions can form hydrates or other Cu complex by combining with polar molecules in the aqueous electrolyte[29] or they may be reduced to Cu^0 by accepting electrons. Consequently, a fluid-like amorphous interphase of Cu complex with a mixture of Cu^0 and Cu^{1+} is formed.

The observed amorphous interphase formation not limited to the ESLI in Cu-catalysed CO_2ER. We have conducted a set of control experiments. For example, an amorphous interphase can also be found at the ESLI without the presence of CO_2 in electrolyte (Supplementary Figs. 37 and 38), which implies that the formation of the amorphous interphase is not exclusive to the CO_2ER. Furthermore, amorphous interphase formation is also found in other materials systems, such as lead (Pb), indium (In) and tin (Sn), in electrolyte under the certain biasing conditions (Supplementary Figs. 39–41). It is noted that the process observed in this study is different from the reported interphase formation during etching processes[30] (for details, see Methods).

Conclusion

With advanced in situ liquid-cell TEM characterizations, our direct imaging has revealed the atomic dynamics of the ESLI during electrocatalytic reactions. It has uncovered the formation of a fluctuating liquid-like amorphous interphase on the metal catalyst surface, and interphase dynamics mediates the catalyst surface restructuring. The atomic dynamics of ESLIs under electrocatalytic reactions provides fresh knowledge on the intermediate formation and catalyst surface restructuring. The surface reconstruction increases the surface features that enable C_2H_4 formation[1], whereas the thickness of the amorphous interphase positively correlates with the selectivity for C_2H_4. Our in situ PLC TEM development enables future possibilities in investigating atomic mechanisms of electrocatalysis in broad materials systems. These efforts may pave the way towards understanding the dynamic atomic structure and function relationships involving ESLIs, laying the foundation for controlling many electrochemical reactions by tuning solid–liquid interfaces.

Online content

Any methods, additional references, Nature Portfolio reporting summaries, source data, extended data, supplementary information, acknowledgements, peer review information; details of author contributions and competing interests; and statements of data and code availability are available at https://doi.org/10.1038/s41586-024-07479-w.

1. Choi, C. et al. Highly active and stable stepped Cu surface for enhanced electrochemical CO_2 reduction to C_2H_4. *Nat. Catal.* **3**, 804–812 (2020).
2. Mefford, J. T. et al. Correlative operando microscopy of oxygen evolution electrocatalysts. *Nature* **593**, 67–73 (2021).
3. Liu, M. et al. Enhanced electrocatalytic CO_2 reduction via field-induced reagent concentration. *Nature* **537**, 382–386 (2016).
4. Zachman, M. J., Tu, Z., Choudhury, S., Archer, L. A. & Kourkoutis, L. F. Cryo-STEM mapping of solid–liquid interfaces and dendrites in lithium-metal batteries. *Nature* **560**, 345–349 (2018).
5. Molinari, A. et al. Hybrid supercapacitors for reversible control of magnetism. *Nat. Commun.* **8**, 15339 (2017).
6. Nel, A. E. et al. Understanding biophysicochemical interactions at the nano–bio interface. *Nat. Mater.* **8**, 543–557 (2009).
7. Egbe, D. I. O., Jahanbani Ghahfarokhi, A., Nait Amar, M. & Torsæter, O. Application of low-salinity waterflooding in carbonate cores: a geochemical modeling study. *Nat. Resour. Res.* **30**, 519–542 (2021).
8. Chen, H. W. et al. Characterizing the influence of water on charging and layering at electrified ionic-liquid/solid interfaces. *Adv. Mater. Interfaces* **2**, 1500159 (2015).
9. Ji, Y. et al. Selective CO-to-acetate electroreduction via intermediate adsorption tuning on ordered Cu–Pd sites. *Nat. Catal.* **5**, 251–258 (2022).
10. Yang, Y. et al. Operando studies reveal active Cu nanograins for CO_2 electroreduction. *Nature* **614**, 262–269 (2023).
11. Li, C. Y. et al. In situ probing electrified interfacial water structures at atomically flat surfaces. *Nat. Mater.* **18**, 697–701 (2019).
12. Wang, Y. H. et al. In situ Raman spectroscopy reveals the structure and dissociation of interfacial water. *Nature* **600**, 81–85 (2021).
13. Favaro, M. et al. Unravelling the electrochemical double layer by direct probing of the solid/liquid interface. *Nat. Commun.* **7**, 12695 (2016).
14. Su, H. et al. Dynamic evolution of solid–liquid electrochemical interfaces over single-atom active sites. *J. Am. Chem. Soc.* **142**, 12306–12313 (2020).
15. Bie, Y. Q. et al. Vibrational spectroscopy at electrolyte/electrode interfaces with graphene gratings. *Nat. Commun.* **6**, 7593 (2015).
16. He, X., Larson, J. M., Bechtel, H. A. & Kostecki, R. In situ infrared nanospectroscopy of the local processes at the Li/polymer electrolyte interface. *Nat. Commun.* **13**, 1398 (2022).
17. Cao, H. et al. Tailoring atomic layer growth at the liquid-metal interface. *Nat. Commun.* **9**, 4889 (2018).
18. Sun, X. et al. Dislocation-induced stop-and-go kinetics of interfacial transformations. *Nature* **607**, 708–713 (2022).
19. Monai, M. et al. Restructuring of titanium oxide overlayers over nickel nanoparticles during catalysis. *Science* **380**, 644–651 (2023).
20. Zhang, Q. et al. Defect-mediated ripening of core-shell nanostructures. *Nat. Commun.* **13**, 2211 (2022).
21. Arán-Ais, R. M. et al. Imaging electrochemically synthesized Cu_2O cubes and their morphological evolution under conditions relevant to CO_2 electroreduction. *Nat. Commun.* **11**, 3489 (2020).
22. Wang, X. et al. Morphology and mechanism of highly selective Cu(II) oxide nanosheet catalysts for carbon dioxide electroreduction. *Nat. Commun.* **12**, 794 (2021).
23. Vavra, J., Shen, T. H., Stoian, D., Tileli, V. & Buonsanti, R. Real-time monitoring reveals dissolution/redeposition mechanism in copper nanocatalysts during the initial stages of the CO_2 reduction reaction. *Angew. Chem. Int. Ed.* **133**, 1367–1374 (2021).
24. Li, Y. et al. Electrochemically scrambled nanocrystals are catalytically active for CO_2-to-multicarbons. *Proc. Natl Acad. Sci.* **117**, 9194–9201 (2020).
25. Liao, Y. Practical electron microscopy and database. https://www.globalsino.com/EM/ (2006).
26. Swift, M. W., Swift, J. W. & Qi, Y. Modeling the electrical double layer at solid-state electrochemical interfaces. *Nat. Comput. Sci.* **1**, 212–220 (2021).
27. Vavra, J. et al. Solution-based Cu^+ transient species mediate the reconstruction of copper electrocatalysts for CO_2 reduction. *Nat. Catal.* **7**, 89–97 (2024).
28. Pike, R. D. Structure and bonding in copper(I) carbonyl and cyanide complexes. *Organometallics* **31**, 7647–7660 (2012).
29. Qi, D., Behrens, H., Lazarov, M. & Weyer, S. Cu isotope fractionation during reduction processes in aqueous systems: evidences from electrochemical deposition. *Contrib. Mineral. Petrol.* **174**, 37 (2019).
30. Peng, X. et al. Identification of a quasi-liquid phase at solid–liquid interface. *Nat. Commun.* **13**, 3601 (2022).

Methods

Chemicals

All chemicals used in this study were commercially available and no further purification was required. These included copper(II) chloride ($CuCl_2$; 99.999%, Aladdin), D-(+)-glucose ($C_6H_{12}O_6$; >99.5%, Aladdin), hexadecylamine ($C_{16}H_{35}N$; 98%, Aladdin), hexane (C_6H_{14}; 99.9%, Sigma-Aldrich), ethanol (CH_3CH_2OH; 99.5%, Sigma-Aldrich), carbon dioxide (CO_2; ≥99.8%), potassium bicarbonate ($KHCO_3$; ≥99.5%), sulfuric acid (H_2SO_4; 99.999%, Aladdin), indium(III) chloride ($InCl_3$; 99.999%, Sigma-Aldrich), lead(II) nitrate ($Pb(NO_3)_2$; 99.999%, Sigma-Aldrich), sodium nitrate (Na_2NO_3; ≥99%, Sigma-Aldrich) and tin(IV) chloride pentahydrate ($SnCl_4{\cdot}5H_2O$; 98%, Sigma-Aldrich). To prepare the solutions, an ultrapure purification system (Milli-Q Advantage A10) was used, which produced deionized water with a resistance of 18.2 MΩ cm.

Preparation of Cu nanowires

For the synthesis of Cu nanowires[31], 17 mg of $CuCl_2$, 50 mg of D-(+)-glucose and 180 mg of hexadecylamine were dissolved in 10 ml of deionized water and sonicated for 30 min at room temperature. The resulting solution was heated in an oil bath at 100 °C with magnetic stirring for 6 h. The Cu nanowires were then isolated by centrifugation at 9,500 rpm for 5 min and washed five times with a hexane/ethanol solvent mixture (1:1 volume).

Preparation of In, Pb and Sn nanoparticles

The In nanoparticles were synthesized using electrodeposition[30]. The working electrode used was a glassy carbon electrode and the electrolyte consisted of 0.5 M sulfuric acid and 0.1 M $InCl_3$. Before the electrodeposition process, the electrolyte underwent deoxidization by blowing nitrogen for 30 min. To ensure an air-free environment, the three-electrode cell was placed inside an airtight box equipped with a wire conduit and a gas-guide tube. The In nanocrystals were synthesized by applying a voltage of −1.2 V (versus saturated calomel electrode) for 1,200 s. Following the electrodeposition, the In particles were transferred for CO_2ER testing.

The electrodeposition of Pb particles followed a similar method, with the exception that the electrolyte was substituted by a mixed aqueous solution of 0.01 M $Pb(NO_3)_2$ and 2 M Na_2NO_3. Furthermore, the applied voltage was set at −0.6 V (versus saturated calomel electrode) and the electrodeposition time was substantially reduced to 120 s.

The Sn nanoparticles were synthesized by an in situ method similar to a previously described method[30]. First, the carbon film on a Cu grid support was subjected to O_2 plasma treatment for 10 s. Subsequently, a droplet of 20 mg ml^{-1} $SnCl_4{\cdot}5H_2O$ aqueous solution was deposited onto the carbon film. The wet grid was then covered with another grid. Once the liquid cell was assembled, it was loaded into the microscope to facilitate Sn nanoparticle growth.

Fabrication of high-resolution electrochemical PLC for in situ TEM

The PLC was fabricated using commercial Cu TEM grids as the starting material (200 square mesh, Electron Microscopy Sciences). The top Cu grid was trimmed on one edge (0.5–1.0 mm width) with a razor blade and both sides of the grids were coated with a 500-nm layer of aluminium oxide by sputtering (ast-sputter, NanoLab at UC Berkeley). Subsequently, a 10-nm-thick formvar polymer film was transferred onto the TEM grids using an established protocol. Then 10-nm-thick platinum interdigital electrodes were deposited onto the bottom grids using e-beam evaporation through a shadow mask (Molecular Foundry, Lawrence Berkeley National Laboratory). The top and bottom grids were then ready for the in situ experiments.

Experimental setup

For in situ experiments, the as-synthesized Cu nanowires (Supplementary Fig. 1) in ethanol were drop-casted onto the electrodes of the bottom grid. After drying under the N_2 protecting gas, the liquid electrolyte (0.1 M $KHCO_3$ electrolyte saturated with CO_2 gas) was loaded. Subsequently, we simply placed the top grid on the bottom grid (Extended Data Fig. 1) and they assembled together by van der Waals forces to form a liquid cell after part of the electrolyte was evaporated. Finally, the cell was transferred onto a custom-made electrical biasing holder for in situ TEM experiments (Supplementary Fig. 2).

The ex situ experiments were performed using a customized H-cell setup. Bicarbonate electrolytes were prepared by bubbling carbonate salt solutions (0.1 M $KHCO_3$) overnight with CO_2. To maintain consistency with the in situ experiments, we used Cu grids with aluminium oxide coatings on both sides, subsequently depositing formvar and carbon films as supports for Cu nanowire catalysts (Supplementary Fig. 7). The Pt working electrode of an H cell was connected only with the carbon film. The formvar and the oxide layers acted as insulators, ensuring that Cu catalytic reactions only occurred on the side of the carbon film. Thus, the Cu grid would not react and dissolve into the electrolyte.

For catalytic performance measurements, the electrode preparation and data collection for the calculation of Faradaic efficiency were carried out precisely, as detailed previously[1].

Electric potential calibration

To overcome the limitation of potential deviation in a PLC two-electrode system, we used two approaches. First, we calculated the difference between the Pt electrode and the reversible hydrogen electrode (RHE) to compensate for the potential deviation caused by charging[23]. To calibrate the potential of the Pt counter electrode (that is, a pseudo reference electrode), its half-wave potential (0 V versus Pt) was compared with the half-wave potential (0.1 V versus Ag/AgCl) in a bulk electrochemical cell. This comparison yielded a calibration of the Pt reference electrode potential: E versus RHE = E versus Pt + 0.728 V, assuming a constant pH of 8. Throughout the manuscript, this calibration was used to measure the potential relative to the RHE. Second, based on electrode polarization characteristics (that is, cathodic potential being more negative than the equilibrium potential and anodic potential being more positive than the equilibrium potential), we inferred that the actual potential was more positive than −1.1 V. We conducted a series of ex situ experiments under varying electric potentials (−1.828 V to −1.228 V versus Pt) to validate our observation of an amorphous interphase (Supplementary Figs. 10–17).

Materials characterization

All in situ TEM experiments were conducted using a ThemIS microscope equipped with a Ceta2 CMOS camera. For low-magnification videos (Supplementary Videos 1–5), the experiments were conducted under 300 kV with a probe current of 1.88 nA. The videos were recorded at a magnification of 300,000×, with an electron dose rate of approximately 2,360 e $Å^{-2}$ s^{-1} for each image. High-magnification videos (Supplementary Videos 6–9) were obtained under a 300-kV accelerating voltage with a probe current of 1.04 nA. Videos were recorded at a magnification of 620,000×, with an electron dose rate of around 6,920 e $Å^{-2}$ s^{-1} for each image.

To avoid beam damage to the amorphous layer, we chose to use the cryogenic electron microscopy method in our ex situ control experiments. For cryogenic (S)TEM characterization, the HAADF image (Fig. 1b) was captured under 300 kV with a probe current of 0.504 pA. The image magnification is 4,000× and it was acquired at an electron dose rate of 1,396 e $Å^{-2}$ s^{-1}. The TEM image (Fig. 1d) was taken under 300 kV with a probe current of 1.04 nA. The image magnification is 620,000× and it was acquired at an electron dose rate of 6,920 e $Å^{-2}$ s^{-1}.

EDS characterization was conducted under 300 kV, using a C2 aperture of 50 mm, a spot size of 7 and probe currents ranging from 0.0117 to 0.9360 nA. The experimental setup included a camera length of 60 mm and a pixel dwell time of 50–100 ms. The resulting image was

obtained at a magnification of 300,000×, with an electron dose rate of approximately 1,541 e $Å^{-2}$ s^{-1}. As our E-cell features Al_2O_3 insulated layers on both sides of the commercial Cu TEM grids, the Cu energy-dispersive X-ray signal induced by scattering effects of such E-cell grid is much weaker in comparison with that of a commercial Cu grid, similar to other metal grids (such as Ti, Au and Mo), as shown in Supplementary Fig. 42.

EELS characterization was undertaken under 80 kV, using the TEAM I microscope equipped with a Gatan K3 camera. The zero-loss peak exhibited a full width at half maximum of 110 meV, and a 10 meV dispersion was used for spectrum collection. The experimental parameters included a beam current of 17 pA, a camera length of 60 nm, a pixel dwell time of 100 ms and a step size of 0.5 nm. The temperature of the sample was maintained at about 100 K.

Quantitative analysis for EELS

We used the multiple linear least squares fitting method to quantitatively analyse the EELS data. Initially, we loaded the spectrum data and performed several preprocessing steps, which involved: (1) aligning the onset of the experimental spectra by shifting them and (2) cropping the spectra to retain only the essential section. The processed results are depicted in the figure. Subsequently, we established the hyperspy model in three steps: (1) incorporating each reference spectra; (2) imposing bounds to constrain the fitting process; and (3) setting the *x* scale and shift as fixed parameters, allowing only the *y* scale to vary. Finally, we conducted compositional measurements on the EELS spectra.

DFT calculations

We performed the DFT calculations using a polarized single-ζ atomic basis set, FHI pseudopotential and Perdew–Burke–Ernzerhof exchange-correlation functional. DFT-D2 was applied to include the interlayer molecular interaction. Along the nanowires, a periodic boundary condition was applied, and vertical to the nanowires, open boundaries were used with a vacuum distance longer than 10 Å. A 1 × 1 × 5 k-mesh was used. The density of mesh was cut off at 80 hartrees. The atomic positions were relaxed until the force on each atom was smaller than 0.01 eV $Å^{-1}$. The surface electrostatic potential was considered in the method of the solvent model. In the inexplicit solvation model, the water dielectric constant was set to 78. The difference in cohesive energy between including inexplicit solvent water and the case without inexplicit solvent water was around 0.1 eV.

We computed the phonon spectra of bulk Cu using the phonopy package. The atoms were further relaxed until the force was less than 0.001 eV $Å^{-1}$. The perturbation of finite displacement was performed in a supercell of 3 × 3 × 3. During the simulations of molecular dynamics, NVTassemble was used in molecular dynamics with a 1 × 1 × 3 supercell. The temperature was set as 1,000 K and the time step was 1 fs.

Controlling of electron-beam effects

Electron-beam irradiation can cause electrostatic charging, local heating and/or ionization owing to electrolyte radiolysis[32]. In our experimental setup, electrostatic charging is unlikely to be important because the Cu nanowires are connected to Pt electrodes and surface charges generated by electron-beam irradiation can thus easily dissipate; this ensures that effects on the charged surface are minimal. Similarly, although electrons incident during irradiation can induce inelastic transitions and, thereby, local heating (which, in turn, can induce structural transformations of nanocrystals[33,34]), these effects have been shown to be negligible when using liquid cells[35]. Ionization resulting from electrolyte radiolysis, by contrast, can have a potentially substantial impact on the investigation of electrochemical processes. Although it is hard to avoid completely, we manage and minimize this effect by controlling the electron-beam dose and using a thin liquid cell.

Our systematic control experiments indicate that, under electron dose less than 6,920 e $Å^{-2}$ s^{-1}, electron-beam effects are not obviously affecting our conclusions drawn from the in situ experiments. Furthermore, the fact that the amorphous interphase is not seen when imaging in the absence of an applied electrical bias (Supplementary Fig. 6) rules out electron-beam effects as the main cause of the observed Cu surface amorphization. Control experiments using different electron-beam doses also showed that a high electron dose and an extended irradiation time are needed for crystalline $Cu(OH)_2$ to appear in the amorphous interphase (Supplementary Figs. 19 and 20), in line with previous studies that reported crystallization of amorphous structure induced by electron-beam irradiation[33]. We accordingly ensured that experiments used electron-beam conditions (for example, an electron current density less than 6,920 e $Å^{-2}$ s^{-1}) that avoided crystallization of the amorphous interphase.

Refrain from bulging

The resolution-reducing bulging issue present in SiN liquid cells[36] is absent in PLCs. For PLCs, we only introduced a small amount of electrolyte (for example, less than 10 μl), which will form numerous small liquid pockets within the liquid cell. Therefore, there is much less electrolyte in each pocket. Also, the hydrolysis reaction occurs simultaneously during electrocatalytic reactions. The generated hydrogen joins the catalytic reaction to generate hydrocarbon products. After an extended catalytic reaction, the amount of electrolyte will decrease, which further reduces the possibility of membrane bulging. Compared with SiN cells, PLCs exhibit sufficiently superior resolution.

Chemical analysis of the amorphous interphase

The chemical composition of the amorphous interphase was examined using both in situ and ex situ experiments (Supplementary Figs. 19–21). The extended electron-beam irradiation induced the formation of Cu_2O and $Cu(OH)_2$ nanocrystals within the amorphous interphase, therefore the interphase contains at least the three elements Cu, O and H.

We also achieved frozen activated amorphous interface by rapidly cooling the PLC using cryogenic TEM technology and then characterized the amorphous interface using EDS and EELS. The EDS spectra (Fig. 1e) show that the amorphous interphase is mainly composed of Cu, C, O and K. The K signal of the amorphous layer is found to correlate with that of the crystalline portion of the frozen sample, suggesting that the K signal comes from the electrolyte (Fig. 1e). The Cu signal shows a substantial increase relative to the background (electrolyte), suggesting the presence of Cu within the amorphous part.

EDS spectra collected over crystalline Cu and amorphous sections show an increase in the carbon-to-oxygen ratio from 59:4 to 84:4 (Supplementary Fig. 43). Because the carbon and oxygen signals in the EDS spectrum of crystalline Cu originate from the polymer film and electrolyte, the larger carbon-to-oxygen ratio in the EDS spectrum collected over the amorphous interphase section suggests that the carbon-to-oxygen ratio of the amorphous interphase itself exceeds that of the polymer film and electrolyte. Given that the presence of oxygen in the amorphous interphase is confirmed (Supplementary Figs. 19–21), this then implies the inclusion of carbon within the amorphous interphase that should thus contain four elements: Cu, C, H and O. EELS spectra (Fig. 1f and Supplementary Table 1) reveal Cu^0 and Cu^{1+} in the amorphous interphase.

Detection of amorphous interphase formation at metal (Pb, In and Sn)–electrolyte interfaces during electrochemical processes

We separately loaded Pb, In and Sn nanoparticles onto the carbon side of the custom-made grid (Supplementary Fig. 7). Given the electrical conductivity of carbon, it serves as an electrode, obviating the necessity for further Pt electrode deposition onto the carbon film. We used the same parameters as in the experiments for the Cu system, including the potential (−1.1 V versus RHE), electrolyte composition (0.1 M $KHCO_3$) and reaction duration (10 min). After reaction, the samples

were transferred to a cryo-holder in a vacuum and then inserted into a transmission electron microscope (ThemIS) for characterization.

Amorphous interphases also found in other systems

To verify the formation and fluctuation of amorphous interphases also present in other systems, we conducted a series of control experiments and molecular dynamic simulations (Supplementary Figs. 32–34 and 37–41). The outcomes from the control experiment using an electrolyte lacking CO_2 imply that the formation of the amorphous interphase is not exclusive to the Cu-catalysed CO_2ER (Supplementary Figs. 37 and 38). The results of control experiments involving alternative metals (Pb, Sn, In, Pt) replacing Cu reveal that the observed phenomenon of the amorphous interphase is correlated with the strength of metal bonds and not solely limited to the Cu material system (Supplementary Figs. 39–41). Theoretical calculations indicate that electron doping is the primary factor causing the amorphization of metal surface atoms (Supplementary Figs. 32–36). The stronger the inherent strength of metallic bonding, the greater the critical surface electron concentration (Supplementary Fig. 44). Specific to the Cu-catalysed CO_2ER, the primary driving force is still surface charging. However, because Cu nanowires are immersed in the electrolyte, molecules and ions in the electrolyte inevitably associate with the Cu, forming some complexes (Extended Data Fig. 7). In conclusion, the phenomenon of amorphous interphase formation and fluctuation at the ESLI is a widespread occurrence.

Stability tests of $KHCO_3$ electrolyte under electron-beam irradiation

We tested the stability of the $KHCO_3$ electrolyte under electron-beam irradiation (Supplementary Fig. 45). The results illustrate that the electrolyte maintains stability across various electron-beam conditions, maintaining integrity even when subjected to a beam dose rate of 7,000 e $Å^{-2}$ s^{-1}. When the beam dose rate exceeds 10,000 e $Å^{-2}$ s^{-1}, the electrolyte initiates decomposition, accompanied by the production of gas bubbles. Given that our test conditions ensure a beam intensity less than 7,000 e $Å^{-2}$ s^{-1}, the electrolyte consistently retains stability throughout our electrochemical process.

Examination of the effects of amorphous interphases on catalytic performance

Our direct observations have shown that the amorphous interphase can mediate the surface reconstruction resulting in a stepped surface (expressed as A-(*hkl*)), which can improve the selectivity of C_2H_4 (ref. 1) (Extended Data Fig. 8). Furthermore, we examined catalytic performance and quantified the corresponding thickness of the amorphous interphase as a function of varied applied potentials and times (Supplementary Figs. 46–50 and Supplementary Tables 3 and 4). The results revealed a positive correlation between the thickness of the amorphous layer and the selectivity of C_2H_4 within a specific range (−0.76 V to −1.07 V versus RHE) in Supplementary Figs. 51 and 52. The performance enhancement may arise from the stepped surfaces, as well as the mixture of Cu^0 and Cu^{1+} ions within the amorphous interphase[1,37]. Under identical biasing conditions (Supplementary Fig. 50), no discernible trend emerges in the thickness of the amorphous interphase over time, which is consistent with the stability of Cu nanowires. Our in situ observations (Extended Data Figs. 3–5 and Fig. 3) also reveal that most of the Cu dissolution and redeposition occur by means of the amorphous interphase acting as an intermediate, rather than directly between solid Cu and the liquid electrolyte (Supplementary Fig. 53).

Differences between electrified interphase and the interphase of metal during etching

In the previously reported etching-induced interphase[30], In (or Sn) metal nanoparticles were obtained in situ using a growth solution by dissolving $InCl_3$ (or $SnCl_4$) in water. The oxidative etching environment (for example, with the presence of HCl or other species) is necessary to produce the amorphous interphase. In the etching environment, the metal surfaces were oxidized to generate metal ions In^{3+}(or Sn^{4+}) and they mixed with Cl^- and OH^- ions to maintain electrical neutrality, resulting in the formation of an amorphous interphase. It is fundamentally different from the ESLIs.

For the formation of electrified amorphous interphase, the metal surface charges is the key. Under negative biasing, the doped electrons weaken the interaction of metal atoms, leading to the destruction of the crystal structure. Simultaneously, the solution molecules react with the activated metal atoms, contributing to the amorphous composition. Details have been reported in the main text.

Data availability

All data generated or analysed during this study are included in the published article and its Supplementary Information files.

31. Jin, M. et al. Shape-controlled synthesis of copper nanocrystals in an aqueous solution with glucose as a reducing agent and hexadecylamine as a capping agent. *Angew. Chem. Int. Ed.* **50**, 10560–10564 (2011).
32. Egerton, R. F., Li, P. & Malac, M. Radiation damage in the TEM and SEM. *Micron* **35**, 399–409 (2004).
33. Nakamura, R., Ishimaru, M., Yasuda, H. & Nakajima, H. Atomic rearrangements in amorphous Al_2O_3 under electron-beam irradiation. *J. Appl. Phys.* **113**, 064312 (2013).
34. Jenčic, Bench, M. W., Robertson, I. M. & Kirk, M. A. Electron beam induced crystallization of isolated amorphous regions in Si, Ge, GaP, and GaAs. *J. Appl. Phys.* **78**, 974–982 (1995).
35. Wang, W. et al. Solid–liquid–gas reaction accelerated by gas molecule tunnelling-like effect. *Nat. Mater.* **21**, 859–863 (2022).
36. Zhou, S. et al. Visualizing interfacial collective reaction behaviour of Li–S batteries. *Nature* **621**, 75–81 (2023).
37. Xiao, H., Goddard, W. A. III, Cheng, T. & Liu, Y. Cu metal embedded in oxidized matrix catalyst to promote CO_2 activation and CO dimerization for electrochemical reduction of CO_2. *Proc. Natl Acad. Sci.* **114**, 6685–6688 (2017).

Acknowledgements This work was supported by the U.S. Department of Energy, Office of Science, Office of Basic Energy Sciences (BES), Materials Sciences and Engineering Division under contract no. DE-AC02-05-CH11231 within the in situ TEM programme (KC22ZH). Work at the Molecular Foundry of Lawrence Berkeley National Laboratory (LBNL) was supported by the U.S. Department of Energy under contract no. DE-AC02-05-CH11231. S.B.B. acknowledges financing from the Alexander von Humboldt Association. We thank D. T. Limmer and S. M. Griffin for useful discussions on the results.

Author contributions Q. Zhang and H.Z. conceived this work. Q. Zhang designed and performed the in situ TEM experiments on CO_2ERs. Q. Zhang, X.S., Y.L. and J.W. performed the ex situ CO_2ER experiment, catalyst characterization and electrochemical test. S.B.B., J.S., J.W., Q. Zhang, X.S. and H.Z. designed and fabricated the electrochemical polymer liquid cell (PLC). Z.S. carried out the calculations, under the supervision of P.N. Q. Zhang and J.W. performed materials synthesis. Q. Zhang, X.S., J.W., Z.S., J.S., Q. Zheng, K.C.B., P.E., P.N., Y.H. and H.Z. carried out the data analysis. Q. Zhang, Z.S., X.S. and H.Z. co-wrote the manuscript, with input from all authors. This work was done under the supervision of H.Z.

Competing interests The authors declare no competing interests.

Additional information
Supplementary information The online version contains supplementary material available at https://doi.org/10.1038/s41586-024-07479-w.

Correspondence and requests for materials should be addressed to Haimei Zheng.

Peer review information *Nature* thanks the anonymous reviewers for their contribution to the peer review of this work.

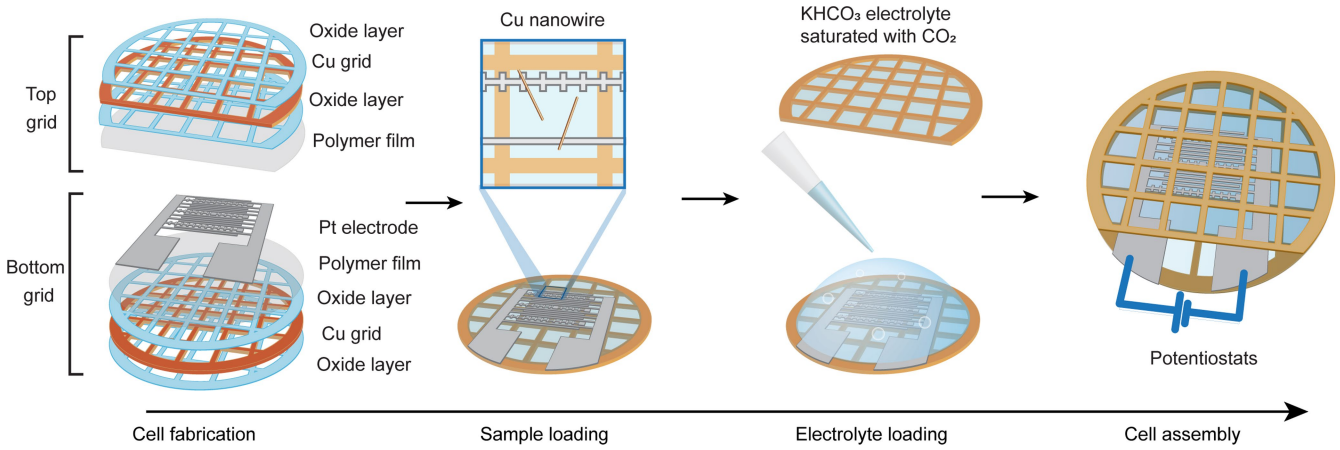

Extended Data Fig. 1 | Experimental setup for in situ HRTEM characterization of the ESLI in an electrochemical PLC. Schematics of the PLC preparation. Top grid, aluminium oxide layers are deposited onto both sides of a truncated Cu TEM grid, followed by the deposition of a polymer film on one side of it. Bottom grid, aluminium oxide layers are applied to both sides of a Cu TEM grid, followed by the sequential deposition of a polymer film and Pt electrodes on one side. After loading the Cu nanowires with $KHCO_3$ electrolyte (0.1 M, saturated by CO_2) onto the bottom grid, it is assembled with the top grid to form an electrochemical PLC. When it is loaded into a TEM electric biasing holder, an electrical potential can be applied to study the ESLI.

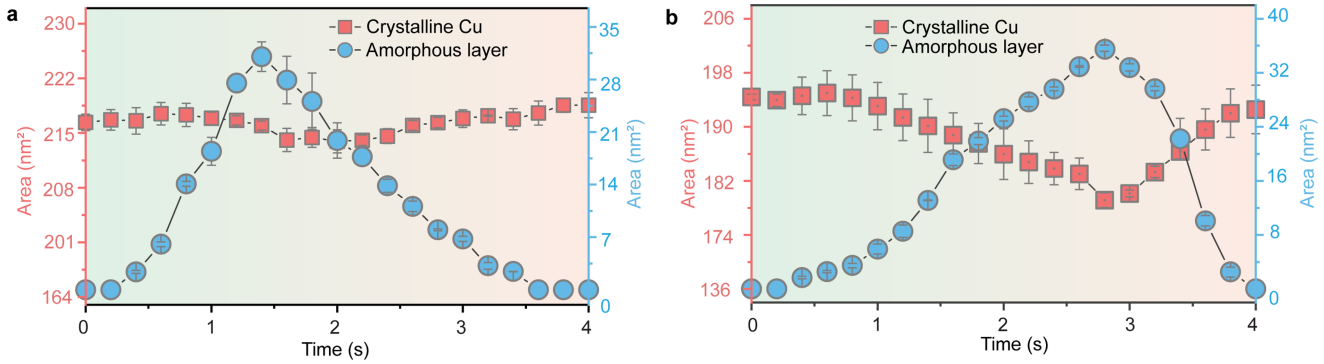

Extended Data Fig. 2 | Quantification of the variations in the projected areas of amorphous interphase and crystalline Cu versus time in the two scenarios. a, Projected areas of crystalline Cu and amorphous interphase over time in the scenario with dominant lateral flow behaviour. **b**, Projected areas of crystalline Cu and amorphous interphase over time showing the dominant interconversion behaviour.

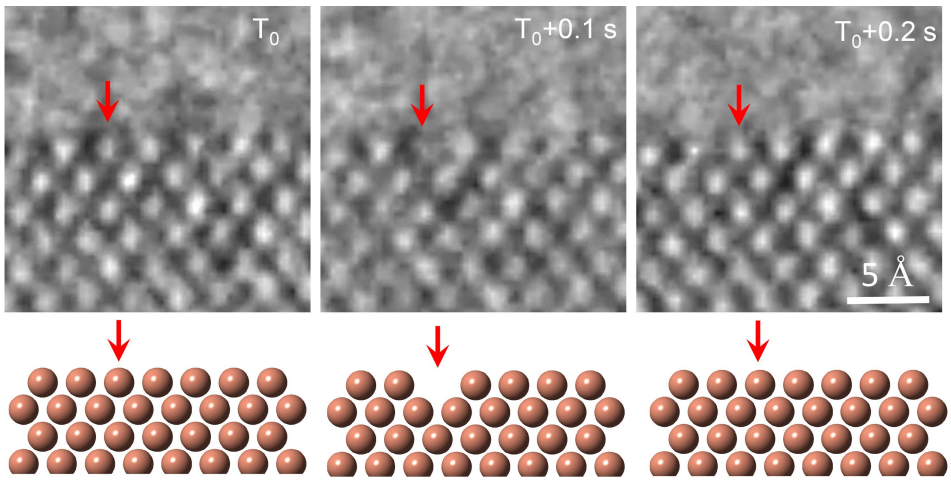

Extended Data Fig. 3 | Forming and refilling of Cu vacancies at crystalline Cu–electrolyte interfaces. Initially, the atomic terrace is intact. After 0.1 s, a single atomic column is extracted, resulting in an atomic vacancy on the terrace. Subsequently, this void is promptly filled by Cu from the solution, thereby reinstating the atomic platform to its original state.

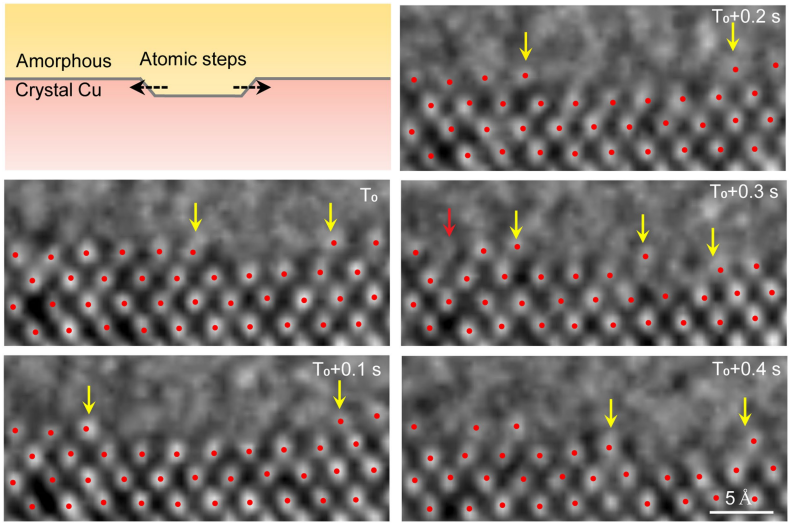

Extended Data Fig. 4 | HRTEM images show the random detachment process of Cu atoms at the crystalline Cu–amorphous interphase interface. In the schematic, the red and yellow sections represent crystalline Cu and the amorphous interphase, respectively. The yellow arrows point to the atoms at atomic step edges. The red arrow points to an atomic vacancy on the terrace.

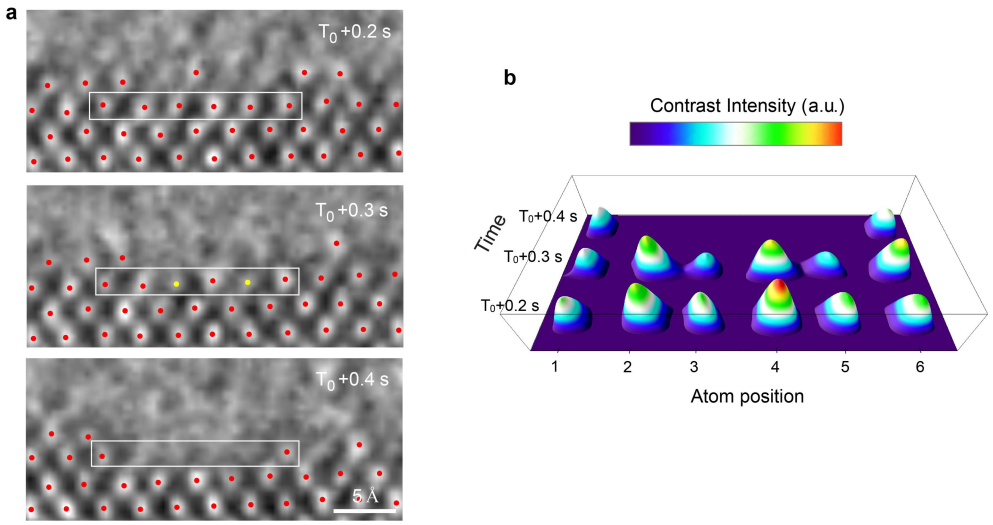

Extended Data Fig. 5 | The contrast of the Cu atom columns becomes weaker during the dissolution process. a, HRTEM images show the dissolution process. The white boxes mark out the focused area. **b**, The contrast intensity of the atomic column in the focused region shows that, at T_0 + 0.3 s, there is dissolution observed in some of the atoms located at positions 3 and 5.

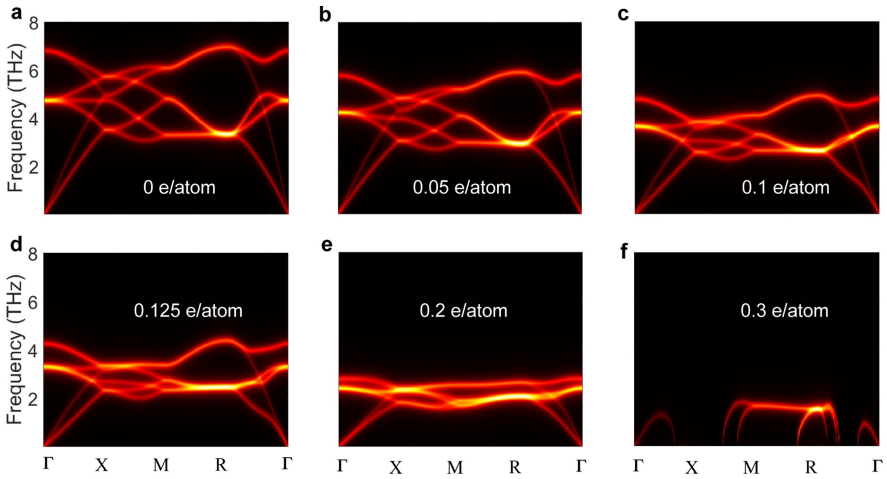

Extended Data Fig. 6 | DFT-calculated phonon band structures of bulk Cu under different doping concentrations. a–**f**, Electron doping varies from 0 to 0.3 e per atom. Γ (0, 0, 0), X (0.5, 0, 0), M (0.5, 0.5, 0) and R (0.5, 0.5, 0.5). The bandwidth of the phonon indicates the mechanical strength.

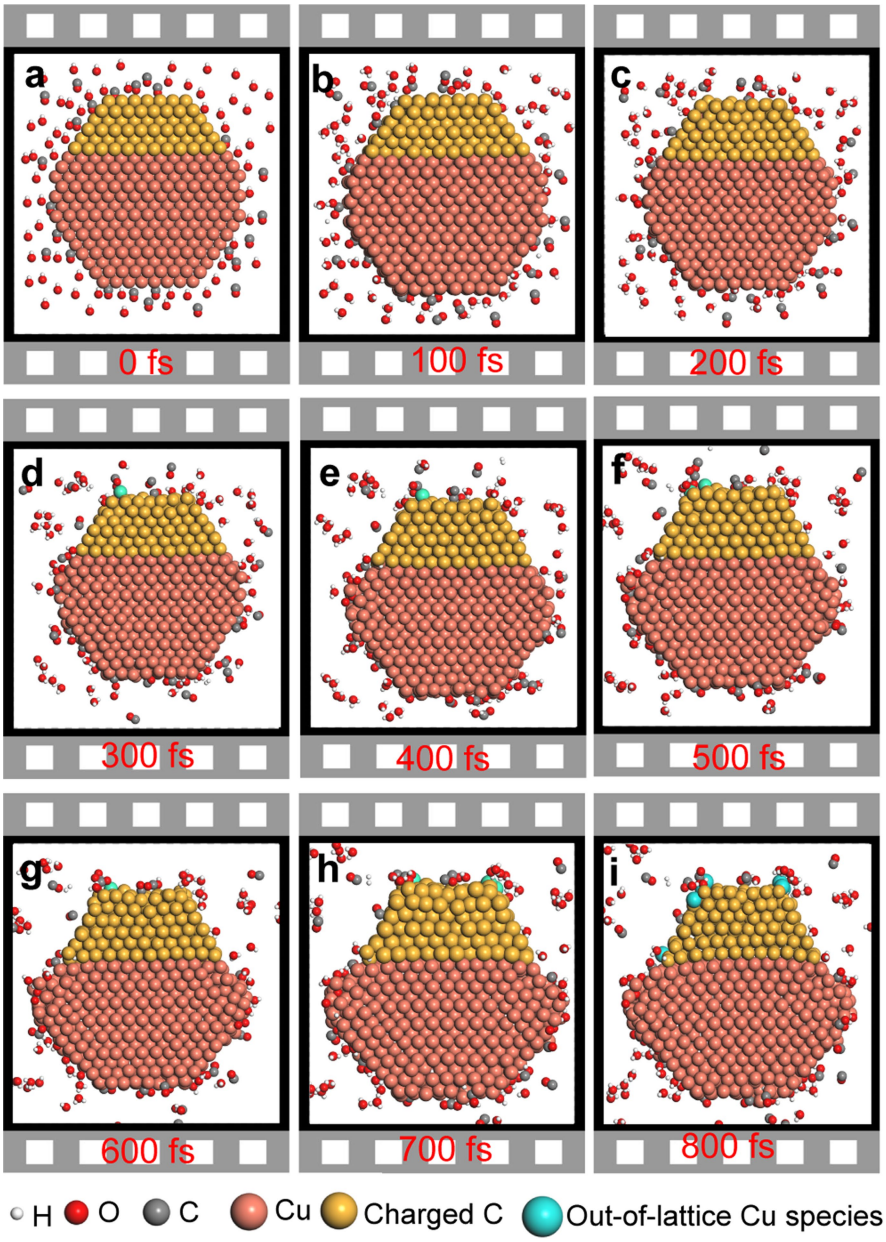

Extended Data Fig. 7 | Images of the molecular dynamic simulation of Cu nanowire surrounded by CO and H_2O. The grey, red, white and light-red balls represent C, O, H and Cu atoms, respectively. The blue balls represent the Cu species out of the crystal lattice. Only crossing views of nanowires are shown. The effect of the electrode is included in the electron distribution induced by electrostatic potential. A large electron concentration of 0.5 e per atom is doped into the upper half part.

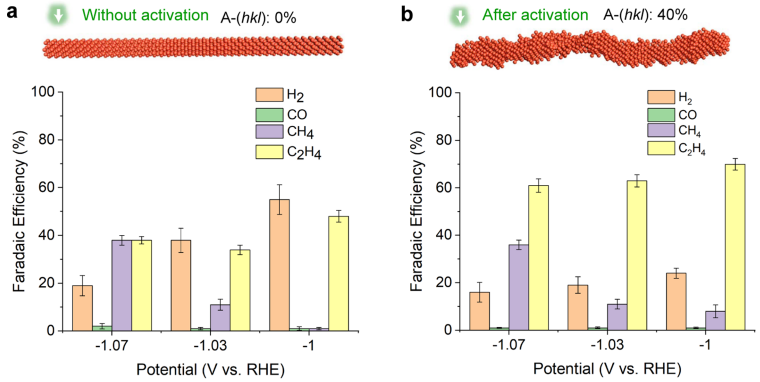

Extended Data Fig. 8 | Electrochemical CO_2 reduction reaction performance of Cu nanowire catalysts before and after activation. a, Faradaic efficiency of the synthesized Cu nanowires. **b**, Faradaic efficiency of the activated Cu nanowires. Data are mean ± s.d. The data presented are the mean values based on three independent measurements; error bars correspond to the s.d.; $n = 3$ independent measurements.